

Efficient Vertical Charge Transport in Polycrystalline Halide Perovskites Revealed by Four-Dimensional Tracking of Charge Carriers

Changsoon Cho¹, Sascha Feldmann¹, Kyung Mun Yeom², Yeoun-Woo Jang^{3,4}, Simon Kahmann^{1,5}, Jun-Yu Huang^{1,6}, Terry Chien-Jen Yang^{1,5}, Mohammed Nabaz Taher Khayyat², Yuh-Renn Wu⁶, Mansoo Choi^{3,4}, Jun Hong Noh^{2,7}, Samuel D. Stranks^{1,5}, Neil C. Greenham^{1*}

¹Cavendish Laboratory, Department of Physics, University of Cambridge, Cambridge, UK.

²School of Civil, Environmental and Architectural Engineering, Korea University, Seoul, Republic of Korea.

³Global Frontier Center for Multiscale Energy Systems, Seoul National University, Seoul, Republic of Korea.

⁴Department of Mechanical Engineering, Seoul National University, Seoul, Republic of Korea.

⁵Department of Chemical Engineering and Biotechnology, University of Cambridge, Cambridge, UK

⁶Graduate Institute of Photonics and Optoelectronics and Department of Electrical Engineering, National Taiwan University, Taipei, Taiwan

⁷Graduate School of Energy and Environment (KU-KIST Green School), Korea University, Seoul, Republic of Korea.

*e-mail: ncg11@cam.ac.uk

Abstract

Fast diffusion of charge carriers is crucial for efficient charge collection within their lifetime in perovskite solar cells. While lateral transient photoluminescence microscopies have been popularly used to characterise charge diffusion in perovskites, there exists a discrepancy between low diffusion coefficients measured to be on the order of $10^{-2} \text{ cm}^2\text{s}^{-1}$ and near-unity charge collection efficiencies achieved in practical solar cells. Here, we reveal hidden microscopic dynamics in halide perovskites through four-dimensional (4D - x, y, z, t) tracking of charge carriers. First, we investigate a method for characterising out-of-plane diffusion of charge carriers applicable to general semiconductors by exploiting the effect of optical self-filtering on external photoluminescence spectra. By combining this approach with confocal microscopy, we discover a strong local heterogeneity of vertical charge

diffusivities varying from 0.006 to 0.3 cm²s⁻¹ in a 3D perovskite film, arising from the difference between intragrain and intergrain diffusion. By contrast, conventional in-plane measurements yield a diffusivity of only 0.02 cm²s⁻¹ in the same film, which is limited by intergrain charge transport. In the out-of-plane direction across the film thickness, our 4D tracking visualises that most charge carriers are efficiently transported through the direct intragrain pathways or via indirect detours through nearby areas with a fast diffusion. Finally, our technique also quantifies significant anisotropy of exciton diffusion in a vertically stacked 2D perovskite film. The observed anisotropy and heterogeneity of charge carrier diffusion in perovskites rationalize their high performance shown in real devices. Our work also foresees that further control of polycrystal growth will enable solar cells with micrometres-thick perovskites to achieve both long optical path length and efficient charge collection simultaneously.

Keywords: Metal halide perovskite, photon reabsorption, charge carrier diffusion, exciton diffusion, photoluminescence microscopy, four-dimensional tracking of charge carriers, vertical charge transport, anisotropic diffusion, local heterogeneity of diffusivity

Introduction

The diffusion of charge carriers plays an important role in solar cells, to transport holes and electrons across photoactive layers. Among various techniques for characterizing diffusivity,¹⁻⁷ photoluminescence (PL) microscopy is a popular and straightforward method to visualize the diffusive motion of charges. Several groups have used this technique to quantify free charge carrier diffusivities (D_n) of three-dimensional (3D) perovskite films and reported those to be in the order of $10^{-2} \text{ cm}^2\text{s}^{-1}$,^{5,8,9} 1 – 2 orders lower than those for perovskite single crystals^{5,9-11}. With such low diffusivities, charges are expected to take longer than 100 ns to travel across typical perovskite thickness ($\sim 500 \text{ nm}$) in perovskite solar cells (PSCs). Although drift due to internal electric fields can assist carrier extraction at short circuit, these fields are greatly reduced under forward bias, for example close to the maximum power point where cells are operated. Since these travel times are comparable to carrier lifetimes in 3D perovskites (in order of $10^{-7} - 10^{-6} \text{ s}$),^{2,12} a considerable proportion of the charge carriers should be lost through recombination before reaching the electrode at the opposite side, as will be detailed later. This is contrary to the fact that most of high-efficiency PSCs are already achieving high photocurrent densities and fill factors, implying near-unity charge collection efficiencies in both *n-i-p* and *p-i-n* architectures.^{13,14}

We attribute this discrepancy to an insufficient understanding of nanoscale charge dynamics in perovskites. Since polycrystalline perovskite films consist of grains of size hundreds of nanometres, typical PL microscopy has insufficient spatial resolution to fully resolve the effect of grains on the lateral diffusion. Moreover, the majority of perovskite optoelectronics are based on vertical diode stacks sandwiched by two electrodes, where charges travel across the submicron scale thickness in a direction that cannot be tracked by conventional microscopies.

To extend the study of charge carriers in perovskites beyond such limitations, we investigate an analysis based on the self-filtering effect of photoluminescence, which can track the out-of-plane diffusion of dipoles in general semiconductors.^{15,16} The integration of this approach with confocal microscopy enables a spatial mapping of out-of-plane diffusivities and 4D (x, y, z, t) tracking of

charge carriers. In 3D perovskites, the analysis reveals a strong local heterogeneity and anisotropy of charge diffusion, accounting for efficient charge transport occurring in PSCs despite low in-plane diffusivities. The method also uncovers a strong anisotropy of exciton diffusion in 2D perovskites.

Influence of spatial dipole distribution on the external photoluminescence spectrum

As shown in Figure 1a, when a semiconductor film is excited by a short-wavelength laser, photoexcitation occurs predominantly near the surface closest to the incident laser. The PL spectrum collected in reflection mode (R-mode) should be similar to the internal PL spectrum. On the other hand, if the film has a reabsorption length for PL comparable to the thickness, the PL in transmission mode (T-mode), collected from the opposite surface, undergoes a self-filtering. Since the reabsorption is typically larger for high-energy photons with short wavelengths, the self-filtering results in a red-shift of the spectrum.^{13,15-17} When free charge carriers or excitons diffuse into deeper regions of the material, the red-shift in the T-mode is reduced, while a red-shift in the R-mode starts to appear. Both spectra converge once the internal PL becomes uniformly distributed over the thickness. Figures 1b-d show an example based on a 600 nm-thick spin-coated 3D FAPbI₃ (FA: formamidinium) perovskite film. The transient PL spectra were collected by an intensified charge-coupled device (ICCD) camera. Due to the short reabsorption lengths at wavelengths below 800 nm (Figure 1b), initially the bluer shoulder of the normalised PL in the T-mode is suppressed compared to the R-mode (Figure 1c-d). The two spectra approach each other as the charge carriers diffuse at larger times, t . Such symmetrical transient responses in the R-mode and T-mode show that the external spectral change for this film is dominated by optical self-filtering, at least on the nanosecond time scale under investigation. Accordingly, we can correlate the diffusion of charge carriers with the transient PL spectrum, excluding other dynamics potentially affecting the spectrum, which occur several orders faster (fs-ps scale; e.g. charge thermalisation) or slower (ms-s scale; e.g. ion migration and Joule heating) than diffusion.¹⁸

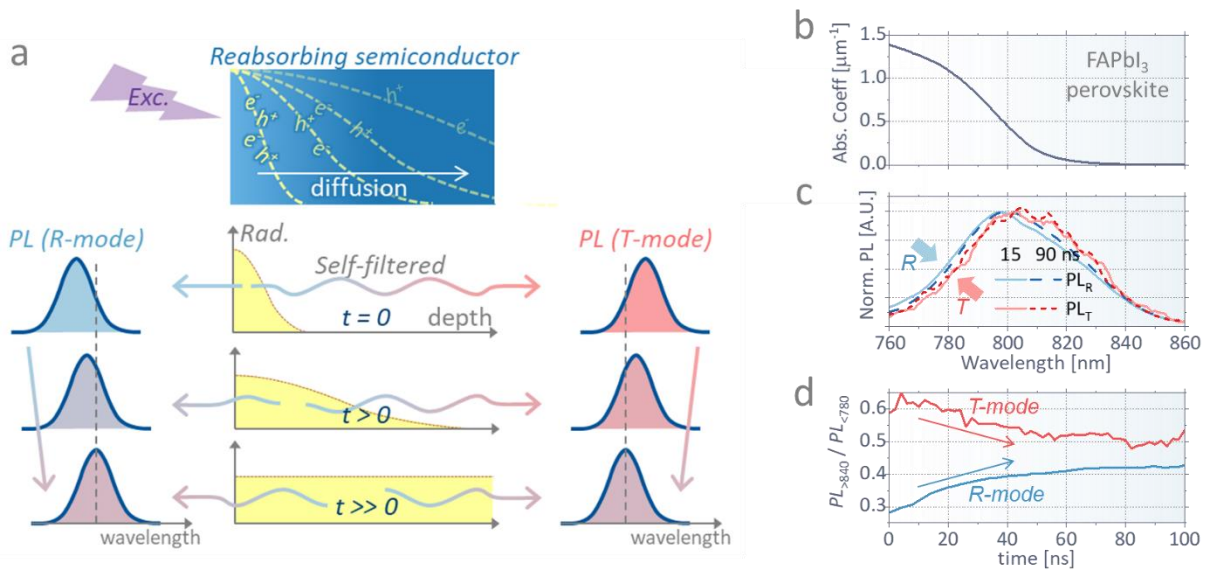


Figure 1. Self-filtering effect on transient PL spectrum of semiconductors. **a**, Transient change of the external PL spectrum collected in reflection (R) and transmission (T) modes. Initially, PL in the T-mode is more red-shifted than the R-mode, as photons near the illuminated surface undergo large reabsorption at short wavelengths. The spectra converge as the charge carrier or exciton profile becomes spatially uniform at long t . **b**, The measured absorption coefficient of our 600 nm-thick FAPbI₃ perovskite film prepared by spin-coating. **c**, Normalised PL spectra of the film measured by ICCD in R-mode and T-mode at 15 ns and 90 ns after the excitation. **d**, The transient variation of the ratio of PL counts at long wavelength (>840 nm) over those at short wavelength (<780 nm).

Characterisation of the out-of-plane charge carrier diffusion

The transient PL spectrum can be analysed to quantify the vertical carrier diffusion across the film. Figure 2a shows our setup for confocal transient PL analysis. A film is illuminated confocally by a pulsed laser. The PL is collected in reflection mode through the same objective and spatially scanned with a Galvano mirror system and a pinhole. The signal is subsequently split before entering two time-correlated single-photon counting (TCSPC) detectors. One is equipped with an optical long-pass

filter (> 800 nm, for PL1) and the other with a short-pass filter (< 800 nm, for PL2) having transmission spectra shown in Supplementary Figure 1.

Figure 2b shows an example of the signals collected at the centre of the beam spot on the FAPbI₃ perovskite. Due to the self-filtering effect, PL2 drops more rapidly at $t > 0$ than PL1, resulting in the initial rise of PL1/PL2 (i.e. red-shift) in Figure 2c. The rise saturates and PL1/PL2 converges to 0.775 at large t , implying that a uniform charge carrier profile is reached. In this manuscript, we use a single carrier density, n , to represent the density of electrons and holes, without attempting to distinguish the populations and diffusivities of electron and hole separately (Supplementary Note 1). The time elapsed for charges to travel across the film thickness (d_{film} , 600 nm) can be roughly approximated by an intersection (τ_{cross} , 80 ns) of the two asymptotes of the curve as shown in Figure 2c. Since the vertical diffusivity is proportional to $\Delta z^2 / \Delta t$ (z : depth), it becomes:

$$D_{n,\text{verti}} = P \times (d_{\text{film}})^2 / \tau_{\text{cross}}. \quad (1)$$

We empirically determine the proportionality constant P by simulating 3D free charge carrier dynamics with diffusion and calculating the externally measured spectra using ray optics, as detailed in Methods section. As shown in Figure 2c, using a charge diffusivity of $0.011 \text{ cm}^2\text{s}^{-1}$ in the model results in a PL1/PL2 curve with τ_{cross} of 80 ns, which is well matched with the experimental response. That gives a value of $P = 0.25$ in equation 1, as further confirmed by cases with various modelled diffusivities (Supplementary Figure 2a). Since in 3D perovskites the radiative recombination is bimolecular ($R_{\text{bi}} \sim n^2$), the distribution of internal emissive dipoles has an effective diffusion constant that is half that of the charge carriers, i.e. $D_{\text{PL,verti}} = 0.5 \times D_{n,\text{verti}}$ and $P = 0.125$ for dipole diffusion.³ The ratio of PL1/PL2 can be directly translated into the internal spatial profile of the dipoles. Based on the results of full diffusion models (Supplementary Figure 2b), we approximate the internal radiation profile with a 1D Gaussian distribution¹⁶:

$$\text{PL}(z) \sim \exp(-z^2 / 2\sigma_{\text{verti}}^2), \quad (2)$$

where σ_{verti}^2 is a variance. Supplementary Figure 2b and 7a show that the Gaussian approximation can reasonably represent the internal radiation profiles in response to the charge diffusion, in the absence of very strong quenching at surfaces. Then PL1/PL2 can be calculated for each Gaussian profile using a ray-optics calculation, giving a one-to-one relationship between PL1/PL2 and σ_{verti} as detailed in Supplementary Note 2 and Supplementary Figure 3. In the calculation, the PL1/PL2 measured at long t (e.g. 0.775 in Figure 2c) is assumed to be the response from the dipoles uniformly distributed over the film, which is used for normalisation. Figure 2d shows the transient change of σ_{verti} obtained from the measured PL1/PL2. It is notable that the short absorption depth (~ 70 nm) for our laser excitation (404 nm) allows precise determination of σ_{verti} in our method, on a lengthscale smaller than typical diffraction limits of hundreds of nanometres in optical microscopy. The variance σ_{verti}^2 increases linearly with t , showing that the linear diffusive motion is dominant over superdiffusion or subdiffusion processes^{6,19,20} in this film. After ~ 150 ns, determination of σ_{verti}^2 becomes unstable since PL1/PL2 is already near the saturation point. The dipole diffusivity ($D_{\text{PL,verti}}$) can be obtained as^{3,10,21}

$$D_{\text{PL,verti}} = \Delta(\sigma_{\text{verti}}^2) / 2\Delta t, \quad (3)$$

where $D_{\text{n,verti}} = 2 \times D_{\text{PL,verti}}$. The $D_{\text{n,verti}}$ from the initial slope of σ_{verti}^2 is shown to be $0.011 \text{ cm}^2\text{s}^{-1}$, consistent with the result from equation 1, validating our calculation. In addition to the direct diffusion of charges, photon recycling can redistribute PL over long distances via photon propagation and reabsorption.^{3,13,22,23} The diffusivity can be also overestimated if bimolecular recombination is dominant at the excited spot where n is large and causes a shorter PL lifetime than in remote areas where n is smaller.^{3,13} Both mechanisms are intensity-dependent in 3D perovskites and affect the apparent diffusivities. However, Figure 2d shows that our $D_{\text{n,verti}}$ is virtually unchanged for various excitation densities. This shows that the measured diffusivity is an intrinsic semiconductor property at the given spot and is not significantly affected by the additional effects mentioned above. For further details, Supplementary Note 1 and Supplementary Figure 4-8 investigate several external factors potentially affecting the proposed analysis, including photon recycling, laser intensity, surface recombination, and charge balance.

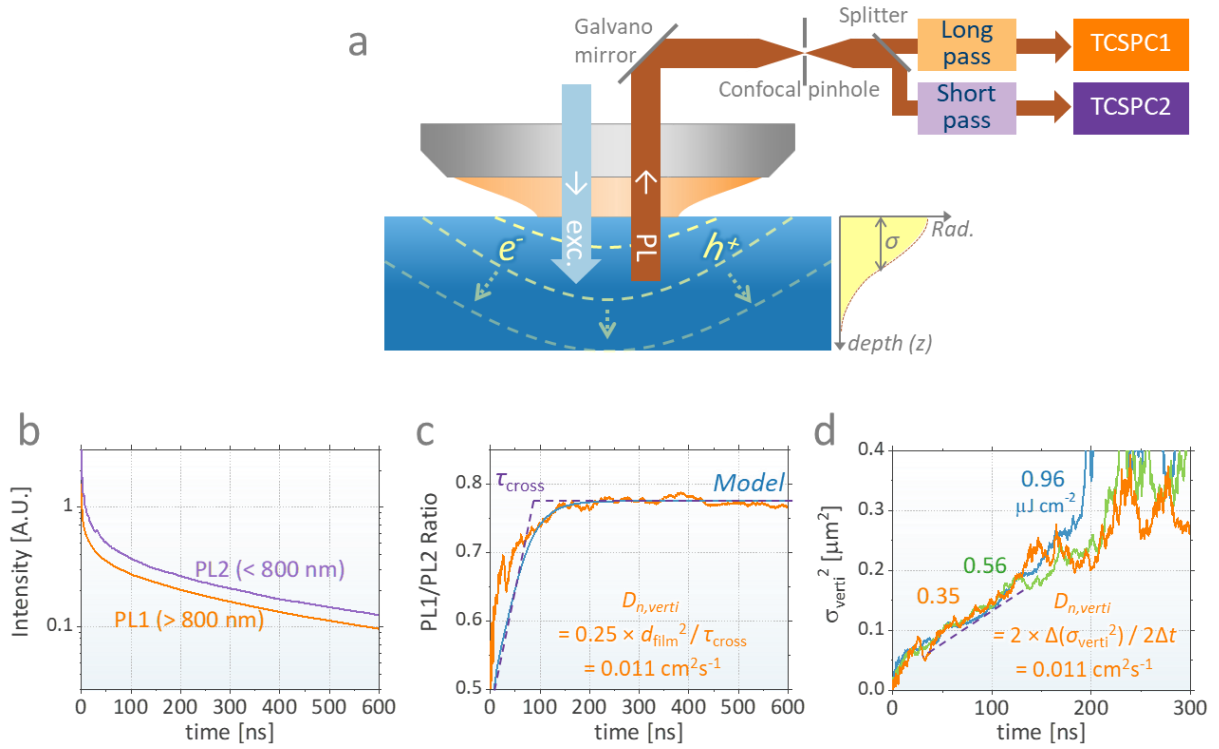


Figure 2. Characterisation of the out-of-plane charge diffusion across the FAPbI₃ perovskite

film. a, Confocal TCSPC setup used in our experiments. PL is excited and collected in R-mode through the same objective. The collected PL is split into two TCSPC detectors having a long-pass filter (> 800 nm, PL1) and short-pass filter (< 800 nm, PL2), respectively. **b,** Measured transient PL1 and PL2 under confocal excitation by a 404 nm laser (200 kHz, pulse width ~ 0.1 ns, $0.35 \mu\text{J cm}^{-2}$ /pulse for an effective beam diameter of $1 \mu\text{m}$). **c,** Transient change of the measured PL1/PL2 ratio (orange), fitted by a charge diffusion model (blue, input diffusivity of $0.011 \text{ cm}^2\text{s}^{-1}$). τ_{cross} of 80 ns is obtained from the two asymptotes and used to estimate $D_{n,\text{verti}}$. **d,** Spatial variance of the internal radiation position along the z-axis (σ_{verti}^2) calculated from the PL1/PL2 ratio assuming the 1D Gaussian distribution. The slope of σ_{verti}^2 results in $D_{n,\text{verti}}$ of $0.011 \text{ cm}^2\text{s}^{-1}$, consistently over the various excitation intensities of 0.35, 0.56, and $0.96 \mu\text{J cm}^{-2}$ /pulse.

Spatial heterogeneity of vertical diffusivity in 3D perovskites

Figure 3 shows results for the spatial mapping of vertical diffusivity in the FAPbI₃ perovskite film using the approach discussed above, where both excitation and collection are scanned together. As shown in Figure 3a-b, the film exhibits a large grain-to-grain variation in the radiation intensity (PL1 integrated over 0 – 650 ns) and bulk PL lifetime (fitted over 170 – 600 ns), which can come from the non-uniform distribution of materials properties such as stoichiometry and defect densities^{12,24-27}. By applying equation 1 to each pixel, we could reveal a strong spatial heterogeneity of $D_{n,verti}$ in the perovskite (Figure 3c), resulting in a laterally varying vertical charge distribution for $t < 100$ ns (Supplementary Figure 9). As an example, we selected two spots with high (“A”) and low (“B”) $D_{n,verti}$ to compare their PL1/PL2 ratio and σ_{verti}^2 as shown in Figure 3d-e. While the PL1/PL2 ratio of A saturates within only a few ns ($\tau_{cross} = 3.5$ ns; $D_{n,verti} = 0.26$ cm²s⁻¹), it takes much longer at B ($\tau_{cross} = 150$ ns; $D_{n,verti} = 0.006$ cm²s⁻¹), exhibiting clearly different slopes of σ_{verti}^2 with time.

Figure 3f plots the distribution of $D_{n,verti}$ over the given domain, which can be approximated by the sum of two distinct Gaussian curves peaking at 0.041 and 0.25 cm²s⁻¹, respectively. While such variation in $D_{n,verti}$ is large compared to that of the PL intensity and lifetime in Figure 3a-b, we could not find a direct correlation between the diffusivity and PL intensity or lifetime. For example, while several works have investigated the influence of trap sites on the carrier diffusivities,^{10,28,29} here region B with slower diffusion exhibits an even longer bulk PL lifetime (~620 ns) than A (~520 ns), indicating that trap density variation is not sufficient to explain the heterogeneous vertical diffusivities observed in Figure 3c. Instead, we propose a hypothesis that the vertical diffusivity is mainly determined by the morphology of the grains. Scanning electron microscope (SEM) cross-section images in Figure 3g and Supplementary Figure 11 show the presence of multiple grains within the thickness of the film in certain regions. In such vertically disconnected regions, the grain boundaries can work as an energy barrier for the charge carriers, hindering their diffusion.^{3,5,24,30,31} Therefore, the two groups of $D_{n,verti}$ values shown in Figure 3f can be understood as areas where vertical diffusion is

predominantly intragrain (e.g. “A”) and areas where diffusion is limited by intergrain processes (e.g. “B”).

Figure 3h and Supplementary Figure 12 show charge collection efficiencies and device performance of PSCs as a function of $D_{n,verti}$, calculated by a drift-diffusion model (see Methods). While a built-in electric field can cause charge carrier drift and compensate their low diffusivities at short circuit, the photocurrent loss becomes prominent with a forward bias, where the electric field is reduced or even reversed. While the charges in the region A are expected to be still efficiently collected (98.5%) at 0.9 V bias, the collection efficiency is shown to be only 75.7% in region B with a low diffusivity, losing the rest through recombination and limiting fill factors to 62.2%. It is notable that even in an ideal solar cell with a trap-free perovskite and perfectly conductive transporting layers, the bimolecular recombination (k_2 of $7 \times 10^{-11} \text{ cm}^3\text{s}^{-1}$) can still compete with charge transport, resulting in a current loss of 6.3% at 0.9 V in region B, which limits the fill factor to be less than 76.1% for PSCs based on intergrain diffusion. Over the domain we measured (Figure 3c), 64% of pixels are shown to have $D_{n,verti}$ larger than $0.1 \text{ cm}^2\text{s}^{-1}$, corresponding to local charge collection efficiencies higher than 99.8% and 96.2% at 0 and 0.9 V, respectively.

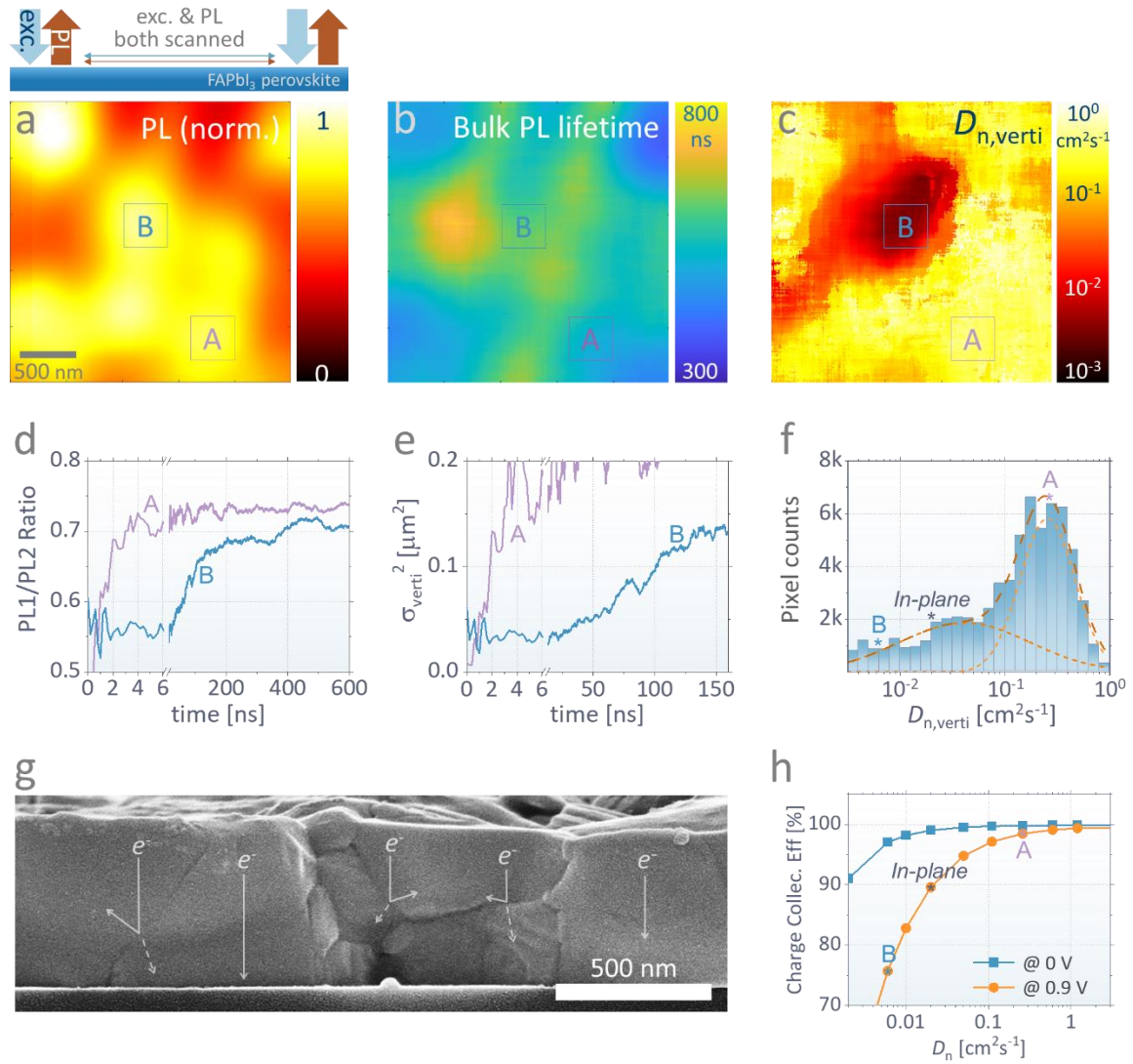


Figure 3. Local heterogeneity of the vertical diffusivity in FAPbI₃ perovskite. **a-c**, Confocal maps of the normalized PL intensity (**a**), bulk lifetime (**b**), and vertical charge diffusivity ($D_{n,verti}$) (**c**), where both confocal excitation and collection are spatially scanned together (excitation: 404 nm, 200 kHz, pulse width ~ 0.1 ns, $1.4 \mu\text{J cm}^{-2}/\text{pulse}$). **d-e**, Transient change of PL1/PL2 ratio (**d**) and σ_{verti}^2 (**e**) of two spots with fast (A) and slow (B) diffusion. **f**, Statistics for number of pixels with each $D_{n,verti}$ in **c**, approximated by the sum of two Gaussian curves with high and low $D_{n,verti}$. The $D_{n,verti}$ values in regions A and B are marked together with an in-plane diffusion coefficient ($D_{n,lateral}$) to be characterised in Figure 4. **g**, Cross-section image of the film obtained using a scanning electron microscope (SEM), showing a schematic for the intergrain and intragrain vertical diffusions. **h**, The calculated charge collection efficiency in practical PSCs at forward bias of 0 and 0.9 V.

Four-dimensional tracking of free-charge carriers

Figure 4a-b show the results for the in-plane tracking of charge carriers in our FAPbI₃ perovskite film. While the position of the pulsed excitation is fixed, the PL is scanned over the whole domain in the x - y plane as depicted at the top of Figure 4a. The measured PL1 broadens laterally with time as shown in Figure 4a. Under the assumption of homogeneous and isotropic diffusion of the Gaussian PL profile, the overall radial diffusivity is obtained to be $D_{n,\text{lateral}} = 0.020 \text{ cm}^2\text{s}^{-1}$, with little dependence on the excitation density (Figure 4b), within the range of the previously reported values for 3D perovskites with similar techniques^{5,8,9}. Supplementary Note 1 and Supplementary Figure 4 show that the contribution of photon recycling is not large in our lateral diffusivity measurement. Comparison with the range of values for vertical diffusivity (Figure 3f) shows that the in-plane diffusivity is in the regime of intergrain diffusion, consistent with intergrain motion being required on the lengthscales probed laterally. A drift-diffusion model based on the laterally measured diffusivity predicts a limited charge collection efficiency of 89.6% at 0.9 V (Figure 3h) and a fill factor of 73.5% (Supplementary Figure 12) in PSCs, inconsistent with the performances of recent state-of-the-art PSCs. Moreover, the brightest point (x,y) of the lateral profile is slightly shifted from (0.85 μm , 0.80 μm) at 1 ns to (1.08 μm , 1.01 μm) at 100 ns in Figure 4a, implying the existence of inhomogeneity in lateral diffusion, similar to what is seen for vertical diffusion.

We now expand our tracking to four dimensions (x, y, z, t). In addition to the lateral tracking, the depth (z) profile of internal radiation can be obtained from the ratio of the measured PL1 and PL2 at each pixel following the procedure described in Figure 2 assuming a Gaussian distribution. The dipole distribution can be converted to the charge profile using the relationship of $n \sim \text{PL}^{1/2}$. Each subfigure in Figure 4c-e shows one vertical and four lateral cross-sections of n , obtained at $t = 1, 5, \text{ and } 100 \text{ ns}$. In the x - z plane the region near $x = 1.3 \mu\text{m}$ (marked with an asterisk) exhibits slow vertical diffusion compared to other areas, indicating the presence of a grain boundary at the middle of the vertical path. Accordingly, when $t = 1$ and 5 ns, in that area n remains more accumulated in the top ($z = 0 \text{ nm}$)

plane, while charges diffuse into the deeper regions in other areas. Such heterogeneity and anisotropy of diffusion can be attributed to the large grain sizes that are comparable to the thickness, such that our film contains areas operating in the intergrain and intragrain regimes. That is contrasted with the same characterisation for a vapour-deposited FAPbI₃ perovskite film, which contains much smaller grains and exhibits isotropic diffusive motion based on intergrain transport for both vertical and lateral directions (Supplementary Figure 13).

Our 4D tracking of charge carriers unveils complicated microscopic dynamics, beyond the limitations of conventional methods. At the top plane ($z = 0$), the centre of the $n(x, y)$ profile is shifted from $x = 1.3 \mu\text{m}$ at 1 ns to $x = 1.0 \mu\text{m}$ at 5 ns, indicating that charges remaining in the top plane due to slow vertical diffusion diffuse laterally to nearby areas in the $-x$ direction. On the other hand, at the deeper planes ($z > 0$), net lateral flows of charge carriers occur in the opposite direction ($+x$) according to the gradient, as represented by the arrows in Figure 4c. The different lateral diffusion behaviours at each depth reveal detours for charge carriers in the areas with low $D_{n,\text{verti}}$ to reach the bottom side through nearby areas providing faster vertical pathways, as depicted by the arrows in Figure 4d.

Figure 4f summarizes the difference between in-plane and out-of-plane diffusions. Since the spatial resolution of optical microscopy is limited by diffraction, typical in-plane diffusion measurements are greatly affected by intergrain charge transport. In contrast, the SEM cross-section images for our perovskite (Supplementary Figure 11) show that 62% of charges at the top surface can be directly transported by intragrain diffusion in the out-of-plane direction. The images also show that 25% of the top surface is vertically disconnected, but obliquely connected to the bottom, allowing fast charge transport through intragrain detours in spite of low local $D_{n,\text{verti}}$. While only 13% of the surface is fully isolated from the bottom area, lateral intergrain diffusion to nearby continuous grains can increase the number of pathways for charge transport to the bottom, making overall diffusion faster than unidirectionally measured $D_{n,\text{verti}}$. The benefit of such heterogeneous diffusivities is further clarified by an illustrative model in Supplementary Figure 14, demonstrating that the lateral charge transport from areas with a low diffusivity to those with a higher diffusivity allows the overall charge collection

efficiency of a heterogeneous system to approach the efficiency for a homogeneous system purely with a fast diffusion.

As a result, in Figure 4g, a practical PSC based on 600 nm-thick FAPbI₃ perovskite exhibits a power conversion efficiency of 23.0% with a high fill factor of 81.8% and external quantum efficiency (EQE) up to 94.5%. The high current density of ~25 mA cm⁻² is maintained at large forward voltage bias of 0.9 V, implying efficient charge transport beyond the performance achievable with a laterally measured diffusivity of 0.02 cm²s⁻¹ (Supplementary Figure 12), proving that more efficient vertical charge transport occurs in the device.

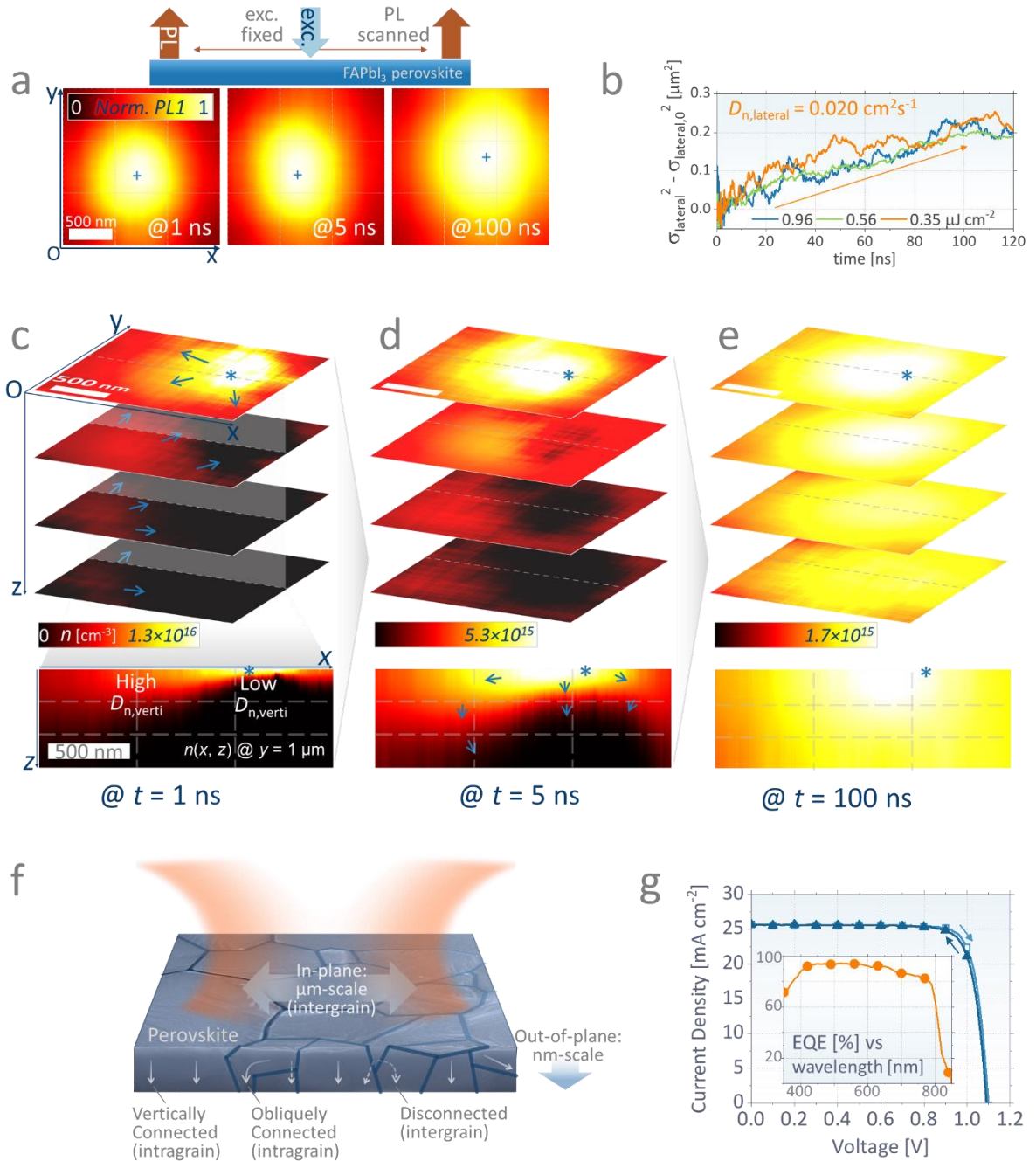


Figure 4. Four dimensional (x, y, z, t) tracking of free charge carriers in FAPbI₃ perovskite. a, Laterally scanned PL1 (normalised) at 1, 5, and 100 ns, under a fixed confocal excitation (excitation: 404 nm, 200 kHz, pulse width ~ 0.1 ns, $0.35 \mu\text{J cm}^{-2}/\text{pulse}$). The brightest spot of each profile is marked by crosses (+). **b,** Radial diffusion of PL1 at various excitations, where $\sigma_{\text{lateral}}^2$ is a lateral variance for the 2D Gaussian approximation. **c-e,** Transient and spatial profiles of free charge carriers ($n(x, y, z, t)$), calculated from the measured PL1 and PL2. The cross-sections are at $z = 0, 200, 400$,

600 nm and $y = 1 \mu\text{m}$, respectively, at $t = 1, 5,$ and 100 ns after the excitation. The asterisks (*) are marked at $(x, y, z) = (1.3, 1.0, 0 \mu\text{m})$ of each image, representing the spot where charges are initially accumulated due to low $D_{n,\text{verti}}$. The arrows indicate the flows of charge carriers parallel to the gradient of n . **f**, A schematic to describe the in-plane and out-of-plane diffusions. For out-of-plane diffusion, both intergrain and intragrain regimes are present, where the vertical intergrain charge transfer can be assisted by nearby continuous grains. **g**, Current density -voltage curves (reverse and forward sweeps, under 1-sun AM1.5G conditions) and external quantum efficiency (EQE) spectrum of a full $n-i-p$ PSC device having FAPbI₃ perovskite as a photoactive layer and antireflection coating on the glass substrate.

Anisotropic exciton diffusion for in-plane stacked 2D perovskites

Our method can also be applied to materials with anisotropic structure, in which out-of-plane diffusion is challenging to measure in thin-films. Figure 5 and Supplementary Figure 15 show data for a BA₂PbI₄ (BA : butylammonium) 2D perovskite, where excitons are bound in the in-plane layers of lead iodide octahedra, which are sandwiched between BA spacer cations with an octahedron-octahedron distance of $\sim 0.7 \text{ nm}$ ^{32,33}. A 6.4° peak in XRD results (Supplementary Figure 15a) stands for the well-formed (002) lateral crystal plane in a direction parallel to the substrate.³⁴ Compared to our 3D perovskite sample, the 2D layers show relatively large lateral grain sizes of several micrometres (Figure 5a). Figure 5b shows symmetric spectral shifts of the PL in R- and T-mode during the initial 30 ns after excitation. The short PL lifetime of the 2D perovskite ($< 5 \text{ ns}$, Supplementary Figure 15c) restricts the measurable time range, and at the latest time measurable, 30 ns, the PL signals in R-mode and T-mode have not yet converged. Figure 5c shows the ratio of PL1 ($> 550 \text{ nm}$) to PL2 ($500 \pm 20 \text{ nm}$), collected by averaging 50 different spots over the film with short light exposures (13 s) at each spot to avoid the photodegradation occurring under long laser exposure. Similar to Figure 5b, PL1/PL2 does not reach τ_{cross} within the time domain of 40 ns in Figure 5c, indicating that the excitons take longer than 40 ns to reach the opposite side of the film. If we take 40

ns as the lower bound of τ_{cross} , the exciton diffusivity ($D_{X,\text{verti}}$) from equation 1 ($P = 0.125$; $d_{\text{film}} = 350$ nm measured with a profilometer) must be less than $0.004 \text{ cm}^2\text{s}^{-1}$. On the other hand, the large lateral sizes of the grains allow faster in-plane diffusion based on the intragrain dynamics ($D_{X,\text{lateral}} = 0.04 \text{ cm}^2\text{s}^{-1}$), as shown in Figure 5d. Such an anisotropy of $D_{X,\text{lateral}}/D_{X,\text{verti}} > 10$ we measure for a thin-film 2D perovskite is much bigger than the recently reported values obtained by directly measuring bulk single crystals, such as 3.7 for $(\text{PEA})_2\text{PbI}_4$ (PEA: phenethylammonium)³⁵ and 1.5 for 4AMP-MAPb₂I₇ (4AMP: 4-(aminomethyl)piperidinium; MA: methylammonium)³⁶. Thin-film 2D perovskite stacks are becoming popular in many applications such as solar cells, LEDs, and lasers, based on their high radiation efficiency and stability.^{34,37-40} Hence accurate quantification of their anisotropic exciton transport will be crucial in understanding their device physics and designing efficient diode structures.

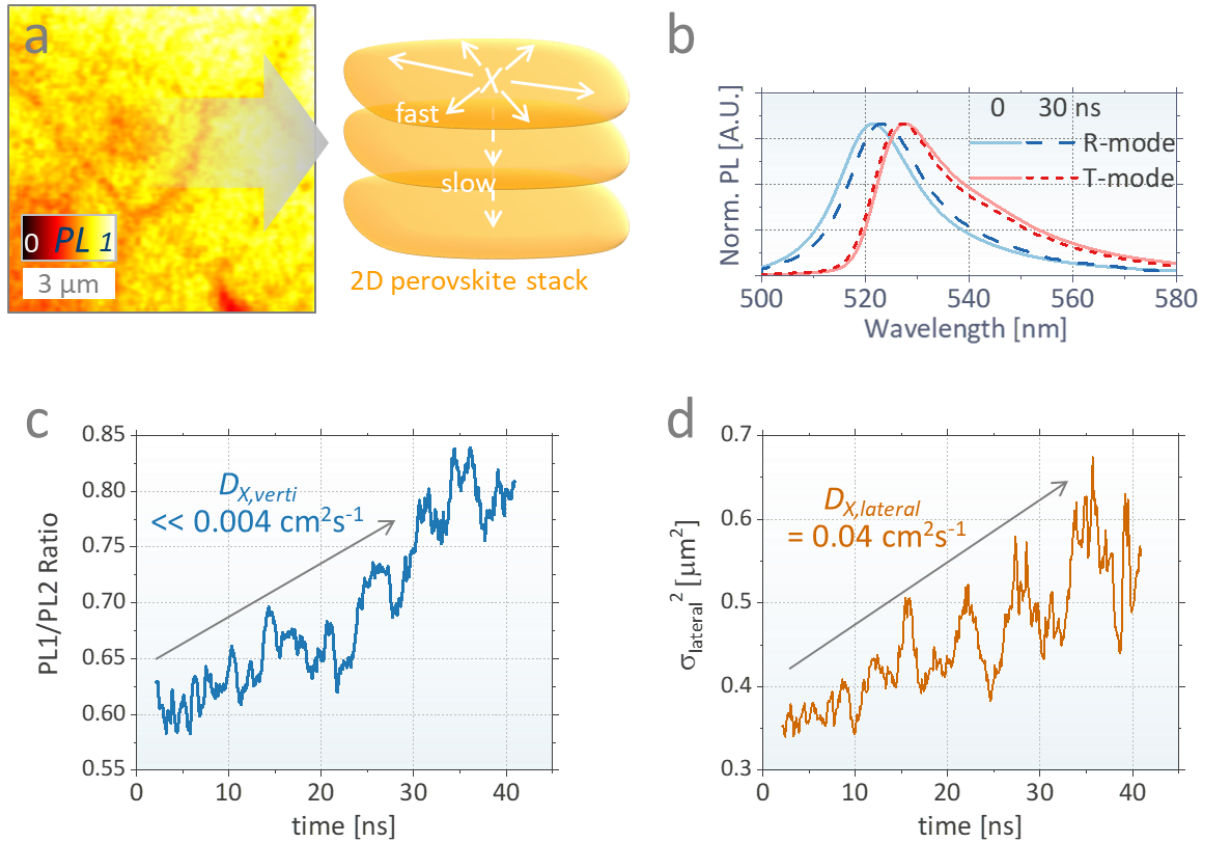


Figure 5. Anisotropic diffusion in a vertically stacked BA_2PbI_4 2D perovskite. a, PL intensity map of the sample having micrometre scale grains (right: schematic to describe the anisotropic exciton (X))

diffusion). **b**, Transient PL spectra in R-mode and T-mode obtained by ICCD. **c-d**, Measured PL1/PL2 ratio (**c**) and lateral spatial variance of PL ($\sigma_{\text{lateral}}^2$, **d**), obtained by averaging 50 different spots over the film (excitation: 404 nm, 5 MHz, pulse width ~ 0.1 ns, $0.046 \mu\text{J cm}^{-2}/\text{pulse}$). $D_{\text{X,verti}}$ and $D_{\text{X,lateral}}$ were calculated according to equations 1 and 3, respectively.

Conclusions

We introduced a method for characterising the vertical diffusivity across semiconductor films, based on the optical self-filtering effect. Using this method, we investigated a strong local heterogeneity of the diffusivities in a 3D FAPbI₃ perovskite film that can be attributed to the difference between intergrain and intragrain diffusion. Through four-dimensional tracking of charge carriers, we investigated the origin of efficient vertical charge transport in PSCs despite the low diffusivities from in-plane measurements. We also characterised the anisotropic exciton diffusion occurring in vertically stacked 2D perovskites.

Understanding diffusion in perovskites is crucial to further developments in PSCs. The performance of current devices exceeds that predicted by many measurements of diffusion coefficients, and our work explains this by providing insights into three-dimensional diffusion at the nanoscale in the presence of inhomogeneity and anisotropy. This opens up possibilities to design PSCs using thicker active layers whilst still achieving efficient charge collection by diffusion. Currently, the optimal thickness of perovskites in solar cells appears to be less than 1 μm scale, limited by their charge transport ability.^{41,42} However, for the future ultrahigh-efficiency devices, thicker active layers are in demand to reduce the efficiency loss from insufficient optical path length, known to be much larger for conventional PSCs than for silicon solar cells,^{43,44} mainly arising at the band-edge region. Increased thickness is also preferential for increasing the benefits of the photon recycling effect¹³ and improving the uniformity in large scale production⁴¹. Based on the fast vertical intragrain diffusivities quantified to be around $0.25 \text{ cm}^2\text{s}^{-1}$, we note that charge carriers can travel over 5 μm in 1 μs , if their path is vertically or obliquely connected to the opposite interface without grain boundaries. The ability to track diffusion in time and

space will stimulate research on controlling the efficient vertical growth of perovskite polycrystals to suppress the formation of vertically isolated grains and achieve efficient charge transport through the micrometre-scale perovskite thickness.

Methods

Sample preparation: The primary sample of 3D FAPbI₃ was prepared by spin-coating (1000 rpm for 5s followed by 5000 rpm for 15s) FAPbI₃ precursor solution (FAI 1.6M, PbI₂ 1.6M, and MAcl 0.45M dissolved in 0.8 ml of DMF and 0.1 ml of DMSO; DMF: dimethylformamide; DMSO: dimethyl sulfoxide) on a fused silica substrate. 1 ml of ethyl ether was dropped onto the substrate at the end of spinning. The film was crystalized through annealing at 150 °C for 10 min, which evaporates MAcl.^{45,46} The sample was encapsulated by attaching a glass substrate on the film. The solar cell was fabricated in a structure of anti-reflection coating/ glass/ fluorine-doped tin oxide (FTO)/ SnO₂/ FAPbI₃ perovskite/ 2,2,7,7-tetrakis-(N,N-di-4-methoxyphenylamino)-9,9-spirobifluorene (spiro-OMeTAD)/ Au, following the literature¹³ by replacing the photoactive layer with FAPbI₃. The control sample of 3D FAPbI₃ with smaller grains used in Supplementary Figure 13 was prepared by a vapour deposition process without MAcl additive. FAI (1.20 Å/s) and PbI₂ (0.60 Å/s) were co-deposited in a vacuum chamber of a Creaphys thermal evaporator system. The film was annealed at 135 °C for 90 min and encapsulated by a thin cover glass with epoxy. The BA₂PbI₄ perovskite was prepared using the hot-casting method, as described in the literature.³⁸

Time-resolved broadband photoluminescence: To measure the photoluminescence (PL) spectra of the perovskite films at a given time delay after photoexcitation, an electrically gated intensified charge-coupled device camera (iCCD, Andor Star DH740 CCI-010) connected to a grating spectrometer (Andor SR303i, 150 lines per mm, blaze 500 nm) was employed. The pulsed output from a mode-locked Ti:Sapphire optical amplifier (Spectra-Physics Solstice, 1.55 eV photon energy, 80 fs pulse width, 1 kHz repetition rate) was used to produce 400 nm excitation via second harmonic generation in a β -

barium borate crystal to photoexcite the samples. A 450 nm short pass filter was used to filter out any residual 800 nm fundamental laser light from the excitation beam. The slit width of the detector was set to 200 μm and no spectral filters were added to the emission beam path so as to not obscure the PL signal in any way. For the time-resolved data, the electrical gate was stepped in 2 ns increments with a 2 ns gate width. For reflection mode detection of PL, the sample was excited at the top face, from which also the PL collection and detection then occurred. For the transmission mode detection of PL, the sample was left unchanged in its position, while the excitation beam now passed it from the bottom face, with the PL collection and detection still occurring from the top face, unchanged and like in the reflection mode.

Absorption coefficients: The absorbance was measured using a UV-vis spectrometer. The offset at long wavelength beyond the bandgap, which comes from reflection or scattering, was subtracted, and the bandedge region was smoothed assuming a constant Urbach energy. The absorption coefficient was obtained from the measured absorbance, considering the thickness of the sample.

Confocal TCSPC: The maps of transient PL were obtained using a confocal TCSPC setup (PicoQuant, MicroTime 200)⁴. A 404 nm pulsed laser (repetition rates of 200 kHz for 3D perovskite and 5 MHz for 2D perovskite) was focused onto the sample with a 100 \times , 0.9 NA objective (MPlanFL N), and separated from the emission signal through a dichroic mirror (Chroma zt405rdc) and 425 nm longpass filter. The emission signal was split into two TCSPC detectors with a 50:50 silver beam splitter and different optical filters (Supplementary Figure 1 for the transmission data), as described in the main text. The collected data was divided by reference data obtained in the same condition but without optical filters, to calibrate the differences in the detectivities and time responses of the two detectors. A Galvano mirror system and confocal pinhole were used for the spatial scan of the excitation and emission, while the excitation spot was fixed in case of the 4D tracking measurement of the charge carriers. The signals were collected for several hours by repeating the sweep (512 \times 512 pixels, dwell time of 100 $\mu\text{s}/\text{px}$), carefully monitoring the stability of the radiation intensity (e.g. photodegradation) and optical focus (e.g. influence of the temperature change). The result was further smoothed by averaging nearby data

points spatially and temporally. The PL intensity map was integrated over the range of $t = 0 - 650$ ns, and the bulk lifetime was calculated by fitting the range of $t = 170 - 600$ ns (the range of transient PL having a simple exponential decay, e.g. in Figure 2b) to an exponential decay function.

Diffusion model: The charge diffusion dynamics was modelled using a custom-made program. A perovskite domain of $2.5 \mu\text{m} \times 2.5 \mu\text{m} \times 600$ nm size was divided into a $50 \text{ nm} \times 50 \text{ nm} \times 20$ nm-sized mesh. The domain was initially excited by 5.6×10^3 photons with a Gaussian distribution ($\sigma_{x,y} = 1.2 \mu\text{m}$, maximum at the centre) along the lateral (x, y) plane and exponential decay ($\alpha_z = 2 \times 10^5 \text{ cm}^{-1}$) along the vertical z -axis, consistently with the experimental condition. The charge carriers (n , not distinguishing electrons and holes) were set to either recombine ($dn/dt = -k_1n - k_2n^2$) or diffuse ($dn/dt = D_n \nabla^2 n$, $D_n = 0.011 \text{ cm}^2\text{s}^{-1}$). The recombination coefficient k_1 of $1.13 \times 10^6 \text{ s}^{-1}$ was obtained from a reciprocal of the measured carrier lifetime (bulk PL lifetime $\times 2 = 890$ ns), while k_2 of $7 \times 10^{-11} \text{ cm}^3\text{s}^{-1}$ is from the literature⁴⁷. The charge carriers were assumed to be reflected at the front and back surfaces without additional surface traps. The external PL1/PL2 ratio was calculated by inputting the calculated internal radiation (k_2n^2) profile to the optical model described below.

Optical model: The top surface emission spectrum was obtained by ray-optical tracing of the internal photons, initially having a preset PL spectrum and isotropic propagation angle. The photons are self-filtered by the perovskite according to the experimentally determined absorption coefficients and Lambert-Beer's law. At each wavelength and each angle for each dipole, light propagation was tracked until it is reabsorbed or outcoupled. Photons are outcoupled or reflected (by Fresnel reflection or total internal reflection) when they meet the front and back surfaces. The effects of photon recycling^{13,17,48} were excluded from our model for simplicity (Supplementary Note 1). Refer to Supplementary Note 2 for further details.

Charge collection model: The charge collection efficiencies were calculated by a full electrical simulation based on a Poisson and drift-diffusion model. The electrical potential profiles are obtained based on the Poisson equation and incorporated into the current continuity equations, as described in the literature in detail.^{49,50} The charge mobilities (μ_n) are assumed to obey the Einstein relation of $D_n =$

$\mu_n V_t$ (V_t : the thermal voltage of 0.026 V at room temperature) ⁵¹ and $D_n = D_p$. A flat 600 nm-thick photoactive layer is assumed to be sandwiched by trap-free transporting layers having charge mobilities of $0.1 \text{ cm}^2\text{V}^{-1}\text{s}^{-1}$, fitted to the experimental data for our photovoltaic device (series resistance $\sim 1.3 \text{ }\Omega\text{cm}^2$). Trap and bimolecular recombination constants of $k_1 = 1.13 \times 10^6 \text{ s}^{-1}$ and $k_2 = 7 \times 10^{-11} \text{ cm}^3\text{s}^{-1}$, respectively, were assumed. For an ideal device, k_1 was set to 0 and the charge transporting layers were assumed to be highly conductive. The charge generation profile was calculated by the finite-difference time-domain method, based on a structure of glass/ FTO (600nm)/ SnO_2 (80nm)/ perovskite (600nm)/ spiro-OMeTAD (260nm)/ Au, with refractive indices from ellipsometry (perovskite) and the literature (others) ⁵². The parameters for electrical simulation are from the literature ⁵², including setting of Gaussian density of state, carrier lifetime, band alignment, and dielectric constant. The electrical simulation was performed with (J_{light}) and without (J_{dark}) AM1.5G illumination. The charge collection efficiency was obtained from the photocurrent density ($J_{\text{ph}} = J_{\text{light}} - J_{\text{dark}}$) at each voltage.

Acknowledgments

This work was supported by the EPSRC (EP/S030638/1). S.D.S. acknowledges the Royal Society and Tata Group (UF150033). the EPSRC (EP/R023980/1, EP/M006360/1), and the European Research Council under the European Union's Horizon 2020 research and innovation programme (HYPERION, grant agreement no. 756962; SOLARX, grant agreement no. 758826). S.F. acknowledges an EPSRC Doctoral Prize Fellowship and is grateful for support from the Winton Programme for the Physics of Sustainability. K.M.Y., K.M.N.T. and J.H.N. acknowledge the National Research Foundation of Korea (NRF) grant funded by the Korean government (MSIP) (NRF-2020R1A2C3009115). J.-Y.H. and Y.-R.W. acknowledge the Ministry of Science and Technology (MOST) of Taiwan under Grant Nos. 109-2221-E-002-196-MY2 and MOST 111-2923-E-002-009. T.C.-J.Y acknowledges the support of a Marie Skłodowska-Curie Individual Fellowship from the

European Union's Horizon 2020 research and innovation programme (PeTSoC, grant agreement no. 891205).

Author contributions

C.C. and N.C.G. conceived the idea. C.C. performed the confocal TCSPC with help of S.K. and S.D.S. C.C. developed the analysis method and performed the diffusion and ray-optics models. S.F. set up and performed the broadband time-resolved PL (iCCD) characterization. K.M.Y. prepared spin-coated 3D perovskite films and took their SEM images under the supervision of J.H.N. Y.W.J. optimized 2D perovskite films and took their XRD patterns under the supervision of M.C. C.C. measured UV-vis transmission. K.M.Y. and K.M.N.T. fabricated and characterized the device under the supervision of J.H.N. J.-Y.H. performed the drift-diffusion model for full devices under the supervision of Y.-R.W. T.C.-J.Y. prepared vapour-deposited 3D perovskite films under the supervision of S.D.S. S.D.S. and N.C.G. supervised the work. All authors discussed the data and contributed to the manuscript.

Competing interests

N.C.G. is a cofounder of a company commercialising perovskite emitters. S.D.S. is a cofounder of Swift Solar.

Data availability

The data underlying this paper are available at [url of Cambridge Apollo repository to be added in proof].

References

- 1 Herz, L. M. Charge-Carrier Mobilities in Metal Halide Perovskites: Fundamental Mechanisms and Limits. *ACS Energy Letters* **2**, 1539-1548 (2017).
- 2 Stranks, S. D. *et al.* Electron-Hole Diffusion Lengths Exceeding 1 Micrometer in an Organometal Trihalide Perovskite Absorber. *Science* **342**, 341-344 (2013).
- 3 deQuilettes, D. W. *et al.* Impact of Photon Recycling, Grain Boundaries, and Nonlinear Recombination on Energy Transport in Semiconductors. *ACS Photonics* **9**, 110-122 (2022).
- 4 Baldwin, A. *et al.* Local Energy Landscape Drives Long-Range Exciton Diffusion in Two-Dimensional Halide Perovskite Semiconductors. *J. Phys. Chem. Lett.* **12**, 4003-4011 (2021).
- 5 Saidaminov, M. I. *et al.* Multi-cation perovskites prevent carrier reflection from grain surfaces. *Nat. Mater.* **19**, 412-418 (2020).
- 6 Seitz, M. *et al.* Exciton diffusion in two-dimensional metal-halide perovskites. *Nat. Commun.* **11**, 2035 (2020).
- 7 Stranks, S. D. Multimodal microscopy characterization of halide perovskite semiconductors: Revealing a new world (dis)order. *Matter* **4**, 3852-3866 (2021).
- 8 Guo, Z., Manser, J. S., Wan, Y., Kamat, P. V. & Huang, L. Spatial and temporal imaging of long-range charge transport in perovskite thin films by ultrafast microscopy. *Nat. Commun.* **6**, 7471 (2015).
- 9 Guo, Z. *et al.* Imaging Carrier Diffusion in Perovskites with a Diffractive Optic-Based Transient Absorption Microscope. *J. Phys. Chem. C* **122**, 10650-10656 (2018).
- 10 Stavrakas, C. *et al.* Visualizing Buried Local Carrier Diffusion in Halide Perovskite Crystals via Two-Photon Microscopy. *ACS Energy Letters* **5**, 117-123 (2020).
- 11 Tian, W. *et al.* Limiting Perovskite Solar Cell Performance by Heterogeneous Carrier Extraction. *Angew. Chem. Int. Ed.* **55**, 13067-13071 (2016).
- 12 de Quilettes Dane, W. *et al.* Impact of microstructure on local carrier lifetime in perovskite solar cells. *Science* **348**, 683-686 (2015).
- 13 Cho, C. *et al.* Effects of photon recycling and scattering in high-performance perovskite solar cells. *Science Advances* **7**, eabj1363.
- 14 Degani, M. *et al.* 23.7% Efficient inverted perovskite solar cells by dual interfacial modification. *Science Advances* **7**, eabj7930.
- 15 Staub, F., Anusca, I., Lupascu, D. C., Rau, U. & Kirchartz, T. Effect of reabsorption and photon recycling on photoluminescence spectra and transients in lead-halide perovskite crystals. *Journal of Physics: Materials* **3**, 025003 (2020).
- 16 Yamada, T., Yamada, Y., Nakaïke, Y., Wakamiya, A. & Kanemitsu, Y. Photon Emission and Reabsorption Processes in CH₃NH₃PbBr₃ Single Crystals Revealed by Time-Resolved Two-Photon-Excitation Photoluminescence Microscopy. *Physical Review Applied* **7**, 014001 (2017).
- 17 Cho, C. *et al.* The role of photon recycling in perovskite light-emitting diodes. *Nat. Commun.* **11**, 611 (2020).
- 18 Li, Z., Chen, Y. & Burda, C. Photoexcited Dynamics in Metal Halide Perovskites: From Relaxation Mechanisms to Applications. *J. Phys. Chem. C* **123**, 3255-3269 (2019).
- 19 Sung, J. *et al.* Long-range ballistic propagation of carriers in methylammonium lead iodide perovskite thin films. *Nature Physics* **16**, 171-176 (2020).
- 20 Guo, Z. *et al.* Long-range hot-carrier transport in hybrid perovskites visualized by ultrafast microscopy. *Science* **356**, 59-62 (2017).
- 21 Zhang, B., Zerubia, J. & Olivo-Marin, J.-C. Gaussian approximations of fluorescence microscope point-spread function models. *Applied Optics* **46**, 1819-1829 (2007).
- 22 Gan, Z. *et al.* The Dominant Energy Transport Pathway in Halide Perovskites: Photon Recycling or Carrier Diffusion? *Adv. Energy Mater.* **9**, 1900185 (2019).
- 23 Pazos-Outon, L. M. *et al.* Photon recycling in lead iodide perovskite solar cells. *Science* **351**, 1430-1433 (2016).
- 24 deQuilettes, D. W. *et al.* Tracking Photoexcited Carriers in Hybrid Perovskite Semiconductors: Trap-Dominated Spatial Heterogeneity and Diffusion. *ACS Nano* **11**, 11488-11496 (2017).
- 25 Feldmann, S. *et al.* Photodoping through local charge carrier accumulation in alloyed hybrid perovskites for highly efficient luminescence. *Nat. Photonics* **14**, 123-128 (2020).
- 26 Frohna, K. *et al.* Nanoscale chemical heterogeneity dominates the optoelectronic response of alloyed perovskite solar cells. *Nat. Nanotechnol* **17** (2021).
- 27 deQuilettes, D. W. *et al.* Photo-induced halide redistribution in organic-inorganic perovskite films. *Nat. Commun.* **7**, 11683 (2016).

- 28 Musiienko, A. *et al.* Deciphering the effect of traps on electronic charge transport properties of
methylammonium lead tribromide perovskite. *Science Advances* **6**, eabb6393.
- 29 Kang, G. *et al.* Electron trapping and extraction kinetics on carrier diffusion in metal halide perovskite
thin films. *J. Mater. Chem. A* **7**, 25838-25844 (2019).
- 30 Arias, D. H., Moore, D. T., van de Lagemaat, J. & Johnson, J. C. Direct Measurements of Carrier
Transport in Polycrystalline Methylammonium Lead Iodide Perovskite Films with Transient Grating
Spectroscopy. *J. Phys. Chem. Lett.* **9**, 5710-5717 (2018).
- 31 Yang, M. *et al.* Do grain boundaries dominate non-radiative recombination in CH₃NH₃PbI₃ perovskite
thin films? *Phys. Chem. Chem. Phys.* **19**, 5043-5050 (2017).
- 32 Ma, C., Shen, D., Ng, T.-W., Lo, M.-F. & Lee, C.-S. 2D Perovskites with Short Interlayer Distance for
High-Performance Solar Cell Application. *Adv. Mater.* **30**, 1800710 (2018).
- 33 Niu, T., Xue, Q. & Yip, H.-L. Advances in Dion-Jacobson phase two-dimensional metal halide
perovskite solar cells. *Nanophotonics* **10**, 2069-2102 (2020).
- 34 Jang, Y.-W. *et al.* Intact 2D/3D halide junction perovskite solar cells via solid-phase in-plane growth.
Nat. Energy **6**, 63-71 (2021).
- 35 Magdaleno, A. J. *et al.* Efficient interlayer exciton transport in two-dimensional metal-halide
perovskites. *Materials Horizons* **8**, 639-644 (2021).
- 36 Shi, Z., Ni, Z. & Huang, J. Direct Observation of Fast Carriers Transport along Out-of-Plane Direction
in a Dion–Jacobson Layered Perovskite. *ACS Energy Letters* **7**, 984-987 (2022).
- 37 Azmi, R. *et al.* Damp heat–stable perovskite solar cells with tailored-dimensionality 2D/3D
heterojunctions. *Science* **376**, 73-77.
- 38 Tsai, H. *et al.* High-efficiency two-dimensional Ruddlesden–Popper perovskite solar cells. *Nature* **536**,
312-316 (2016).
- 39 Ren, Z. *et al.* High-Performance Blue Perovskite Light-Emitting Diodes Enabled by Efficient Energy
Transfer between Coupled Quasi-2D Perovskite Layers. *Adv. Mater.* **33**, 2005570 (2021).
- 40 Qin, C. *et al.* Stable room-temperature continuous-wave lasing in quasi-2D perovskite films. *Nature*
585, 53-57 (2020).
- 41 Chen, J. *et al.* High-Performance Thickness Insensitive Perovskite Solar Cells with Enhanced Moisture
Stability. *Adv. Energy Mater.* **8**, 1800438 (2018).
- 42 Mombiona, C. *et al.* Efficient methylammonium lead iodide perovskite solar cells with active layers
from 300 to 900 nm. *APL Materials* **2**, 081504 (2014).
- 43 Polman, A., Knight, M., Garnett Erik, C., Ehrler, B. & Sinke Wim, C. Photovoltaic materials: Present
efficiencies and future challenges. *Science* **352**, aad4424 (2016).
- 44 impv.amolf.nl/db.
- 45 Mu, C., Pan, J., Feng, S., Li, Q. & Xu, D. Quantitative Doping of Chlorine in Formamidinium Lead
Trihalide (FAPbI₃-xCl_x) for Planar Heterojunction Perovskite Solar Cells. *Adv. Energy Mater.* **7**,
1601297 (2017).
- 46 Jeon, N. J. *et al.* A fluorene-terminated hole-transporting material for highly efficient and stable
perovskite solar cells. *Nat. Energy* **3**, 682-689 (2018).
- 47 Richter, J. M. *et al.* Enhancing photoluminescence yields in lead halide perovskites by photon recycling
and light out-coupling. *Nat. Commun.* **7**, 13941 (2016).
- 48 Cho, C. & Greenham, N. C. Computational Study of Dipole Radiation in Re-Absorbing Perovskite
Semiconductors for Optoelectronics. *Adv. Sci.*, 2003559 (2021).
- 49 Huang, J., Chang, E. & Wu, Y. Optimization of MAPbI₃-Based Perovskite Solar Cell With Textured
Surface. *IEEE Journal of Photovoltaics* **9**, 1686-1692 (2019).
- 50 <http://yrwu-wk.ee.ntu.edu.tw/>.
- 51 Selberherr, S. *Analysis and Simulation of Semiconductor Devices*. (Springer Vienna, 1984).
- 52 Huang, J.-Y. *et al.* Influences of dielectric constant and scan rate on hysteresis effect in perovskite solar
cell with simulation and experimental analyses. *Sci. Rep.* **12** (2022).